


Mapping Single Electron Spins with Magnetic Tomography

Dan Yudilevich,¹ Rainer Stöhr²,³ Andrej Denisenko,² and Amit Finkler^{1,*}

¹*Department of Chemical and Biological Physics Weizmann Institute of Science, Rehovot 7610001, Israel*

^{2,3}*Physikalisches Institut, Universität Stuttgart, Stuttgart 70569, Germany*

 (Received 10 March 2022; revised 27 June 2022; accepted 19 September 2022; published 7 November 2022)

Mapping the positions of single electron spins is a highly desired capability for applications such as nanoscale magnetic resonance imaging and quantum network characterization. Here, we demonstrate a method based on rotating an external magnetic field to identify the precise location of single electron spins in the vicinity of a quantum spin sensor. We use a nitrogen-vacancy center in diamond as a quantum sensor and modulate the dipolar coupling to a proximate electron spin in the crystal by varying the magnetic field vector. The modulation of the dipolar coupling contains information on the coordinates of the spin, from which we extract its position with an uncertainty of 0.9 Å. We show that the method can be used to locate electron spins with nanometer precision up to 10 nm away from the sensor. We discuss the applicability of the method to mapping hyperfine coupled electron spins and show that it may be applied to locating nitroxide radicals. The magnetic tomography method can be utilized for distance measurements for studying the structure of individual molecules.

DOI: [10.1103/PhysRevApplied.18.054016](https://doi.org/10.1103/PhysRevApplied.18.054016)

I. INTRODUCTION

Magnetic resonance spectroscopy (MRS) has been indispensable for determining the structure and function of biomolecules, such as proteins [1,2]. Electron paramagnetic resonance (EPR), for example, is used to study the structure of organic molecules by measuring the distance between two radicals with unpaired electrons attached to predetermined parts of the molecule (i.e., spin labels) [3,4]. Conventional magnetic resonance techniques rely on the signal from large ensembles of molecules and thus measure a mean value. Nanoscale techniques that are sensitive to specific ensemble constituents may augment ensemble techniques and reveal new information.

The nitrogen-vacancy (N-V) center in diamond is an atomic defect in the diamond crystal that can function as a quantum sensor of magnetic fields in nanoscale volumes [5]. Quantum sensing with the N-V center is a promising platform for nanoscale MRS [6], potentially extending the methods down to the single-molecule limit. In recent years, nanoscale nuclear magnetic resonance using N-V centers has been demonstrated [7,8], down to the single-protein level [9], as well as N-V-based EPR spectroscopy of single molecules [10,11].

By mapping the precise positions of spin labels attached to individual organic molecules, it would be possible to elucidate the structure of a single molecule. Mapping the positions of individual electron spins is likewise

relevant for characterizing organic quantum networks, a proposed platform for quantum processors [12]. Such mapping has been demonstrated with magnetic resonance force microscopy [13], scanning tunneling microscopy [14,15], and an N-V-based magnetometer coupled with a scanning magnetic tip [16].

Mapping the positions of nuclear spins is a related endeavor. Recent studies have mapped ¹³C spin clusters in a diamond lattice around an N-V-center sensor based on detecting the Larmor precession of the spins [17–19]. However, this is usually impractical for electron spins due to the similarity between the gyromagnetic factors of the sensor and target spin.

In this paper, we discuss a protocol for locating electron spins in the vicinity of a quantum spin sensor using a varying magnetic field vector, which modulates the dipolar coupling frequency between a target spin and the sensor spin (see Fig. 1). The concept has been proposed for mapping nuclear spins [6], used to map quantum reporter spins on the surface of a diamond for proton magnetic resonance [20] and locating electron-nuclear spin defects within a diamond [21]. Here, we demonstrate that the method can locate electron spins with Ångstrom-scale precision, a ten-fold improvement in accuracy, and discuss its applicability for electron spin mapping.

II. MAPPING PROTOCOL

In our protocol, we measure the dipolar coupling ω_{dd} between the sensor spin and a target spin as a function of the orientation of the external magnetic field (B_0). To do so,

*amit.finkler@weizmann.ac.il

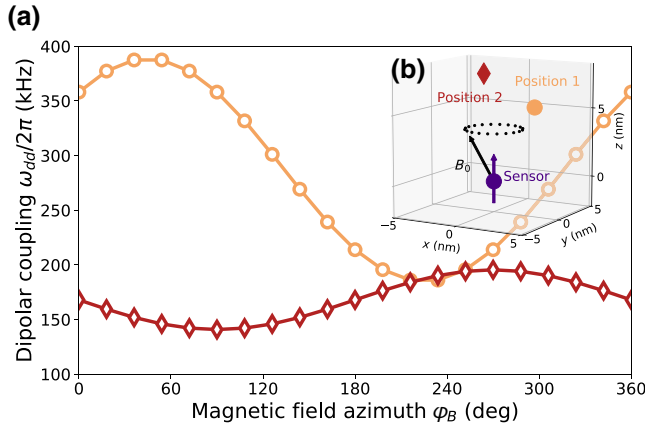


FIG. 1. The simulation of the dipolar coupling frequency modulation by a tilted magnetic field. The curves show distinct dipolar coupling oscillations for two target spin positions. The inset depicts the positions relative to the sensor. The simulation is done for a magnetic field tilted at a polar angle $\theta_B = 29^\circ$ and a varying azimuth φ_B . The amplitude, offset, and phase of the oscillation contain information on the target spin position.

we tilt the magnetic field from the axis of the sensor and sweep along a full 360° trajectory around the axis, analogous to computerized tomography [22]. The orientation of B_0 modulates the dipolar coupling, such that the position of the spin is encoded in the modulation.

We consider a system of a sensor spin (\mathbf{S}_{nv}) with an axial symmetric zero-field splitting (D), coupled to a proximate target spin (\mathbf{S}_e), under an external magnetic field ($\mathbf{B} = B_0 \hat{\mathbf{b}}$). The N-V center in diamond is the archetypal sensor; however, other candidate solid-state spin defects may meet these criteria, e.g., Si-V in SiC [23].

For sufficiently distant spins ($\gtrsim 1.5$ nm) [24], we can approximate the sensor-target spin interaction to a dipole-dipole interaction, denoted by \mathcal{H}_{dd} . We choose our coordinate system such that $\hat{\mathbf{z}}$ is the zero-field splitting axis; γ_{nv} (γ_e) is the sensor (target) spin gyromagnetic ratio. The sensor-target spin system is thus described by the following Hamiltonian:

$$\mathcal{H}/\hbar = DS_{nv}^z + \gamma_{nv} \mathbf{B} \cdot \mathbf{S}_{nv} + \gamma_e \mathbf{B} \cdot \mathbf{S}_e + \mathcal{H}_{dd}/\hbar. \quad (1)$$

We consider a regime where $\mathcal{H}_{dd} \ll \gamma_{nv/e} B_0 \ll D$, so that the eigenstates of the sensor spin are dominated by the zero-field term and the eigenstates of the target spin are dominated by its Zeeman term. We invoke the secular approximation and neglect the components of the sensor and target spin operator that do not commute with $S_{nv}^z = \mathbf{S}_{nv} \cdot \hat{\mathbf{z}}$, $S_e^z = \mathbf{S}_e \cdot \hat{\mathbf{b}}$, accordingly. We obtain the following

approximated term for the dipole-dipole interaction:

$$\begin{aligned} \mathcal{H}_{dd}/\hbar &\approx -\frac{\mu_0 \gamma_{nv} \gamma_e \hbar}{2r^3} \left(3(\hat{\mathbf{z}} \cdot \hat{\mathbf{r}})(\hat{\mathbf{b}} \cdot \hat{\mathbf{r}}) - \hat{\mathbf{z}} \cdot \hat{\mathbf{r}} \right) S_{nv}^z S_e^b \\ &\equiv \omega_{dd}(\mathbf{r}, \hat{\mathbf{b}}) S_{nv}^z S_e^b \end{aligned} \quad (2)$$

$\mathbf{r} = r\hat{\mathbf{r}}$ is the vector connecting the two spins and we define $\omega_{dd}(\mathbf{r}, \hat{\mathbf{b}})$, the field-dependent dipolar coupling strength.

It is convenient to analyze the system in spherical coordinates, where the position of the sensor is set as the origin, and the target position is given by the distance r , a polar angle θ , and azimuth φ . We describe the magnetic field orientation by the polar angle θ_B (the tilt from $\hat{\mathbf{z}}$) and the azimuth φ_B . We then write the dipolar coupling strength as a function of the target spin coordinates and the magnetic field orientation:

$$\begin{aligned} \omega_{dd}(\mathbf{r}, \hat{\mathbf{b}}) &= -\frac{\mu_0 \gamma_{nv} \gamma_e \hbar}{2r^3} \left[(3 \cos^2 \theta - 1) \cos \theta_B \right. \\ &\quad \left. + \frac{3}{2} \sin \theta_B \sin 2\theta \cos(\varphi_B - \varphi) \right]. \end{aligned} \quad (3)$$

For the case of $\mathbf{B} \parallel \hat{\mathbf{z}}$, a field aligned with the axis of the sensor, the second term of Eq. (3) vanishes and the dipolar coupling becomes a function of r and θ alone. However, sampling ω_{dd} at several magnetic field orientations [i.e., several sets of (θ_B, φ_B)] provides information to identify the target spin position.

To extract the available information on the position of the target spin from the dipolar coupling, we consider an experiment where we vary the magnetic field orientation to extract (r, θ, φ) . Equation (3) has the form of a shifted sine, so it is convenient to perform a tomography-like sweep of the azimuth φ_B of the magnetic field at a constant tilt angle θ_B , estimating ω_{dd} at each orientation. ω_{dd} oscillates over φ_B with parameters encoding the position of the spin. The azimuth of the spin φ is encoded in the phase of the sine; the distance r , and polar angle θ , may be extracted numerically by solving a set of nonlinear equations for the offset and amplitude of the sine.

We illustrate a sweep of the magnetic field azimuth for two different target spin positions in Fig. 1, exhibiting distinct sine curves. To extract three variables, three sampling points are sufficient. However, utilizing the added information of the sinusoidal shape will provide a more robust estimation and validate the theory.

III. EXPERIMENTAL RESULTS

We demonstrate single-spin mapping using magnetic tomography on a system composed of a shallow (approximately 8 nm depth) N-V center in diamond as the sensor and a single proximate unpaired electron as the target spin. The target spin is possibly a stable surface spin [16,20,25]

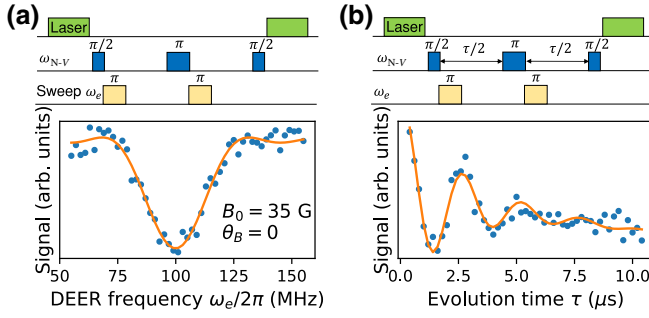


FIG. 2. Measurement of the dipolar coupling of proximate spins with DEER. (a) The top panel depicts the DEER pulse sequence to measure the electron spin resonance of spins proximate to the sensor. The blue dots in the plot are the sensor signal as a function of the DEER frequency ω_e and the orange curve is a fit to squared sinc function. Here, $B_0 = 35$ G and is aligned with the axis of the sensor. (b) The top panel shows the DEER pulse sequence to measure the dipolar coupling strength. We set ω_e to the resonance frequency [obtained in (a)] and the duration of the spin echo τ is varied. The orange line is a fit to a decaying sine.

but its precise nature is unknown. We apply a constant magnetic field (B_0) with a permanent magnet and control the magnitude and direction by moving the magnet. We detect electron spins coupled to the sensor by a double electron-electron resonance (DEER) protocol, which has been discussed in the past in this context [11,16,26,27]. The pulse sequence (see Fig. 2) consists of a spin echo (Hahn) on the sensor spin, decoupling it from the surrounding spin bath to extend the coherence of the sensor [27]. Flipping the target spin midway through the spin echo

couples the evolution of the sensor spin with the field of the target spin. We acquire a resonance spectrum of surrounding spins by sweeping the frequency ω_e of the target spin pulses. Sweeping the duration (τ) of the spin-echo evolution modulates the interaction time and the resulting signal will be modulated according to the dipolar coupling strength of the spins (see Refs. [11,16]; see also the Supplemental Material [28]).

The spin evolution of the sensor is usually affected by a large ensemble of spins (the bath) but due to the r^{-3} scaling of the dipolar interaction, most of the signal originates from a volume of several nanometers radius around the sensor. If there are a few spins in this volume, their dipolar coupling frequencies will dominate, while the distant spin bath will manifest as decoherence [25]. For a single target spin, the signal will oscillate at twice the dipolar coupling frequency (see the derivation in the Supplemental Material [28]).

To map the position of the proximate spin, we estimate the dipolar coupling strength at various orientations of the magnetic field. We measure at a low magnetic field ($B_0 \approx 38$ G) to minimize contrast loss due to a transverse magnetic field [29]. Figure 3 presents the results for a sweep of the magnetic field azimuth $\varphi_B \in [0, 360^\circ]$. In Fig. 3(b), it is apparent that $\omega_{dd}(\varphi_B)$ oscillates over a single period, consistent with Eq. (3). The magnetic field is tilted at an average angle of $\langle \theta_B \rangle = 19.4^\circ$ but the tilt angle θ_B varies over the sweep due to limited control of the magnetic field. We factor in θ_B variation by measuring the value of θ_B with the N-V center for each data point. We then fit the set of measured $\omega_{dd}(\varphi_B, \theta_B)$ to Eq. (3) such that the fit function slightly deviates from a smooth sine shape as expected if

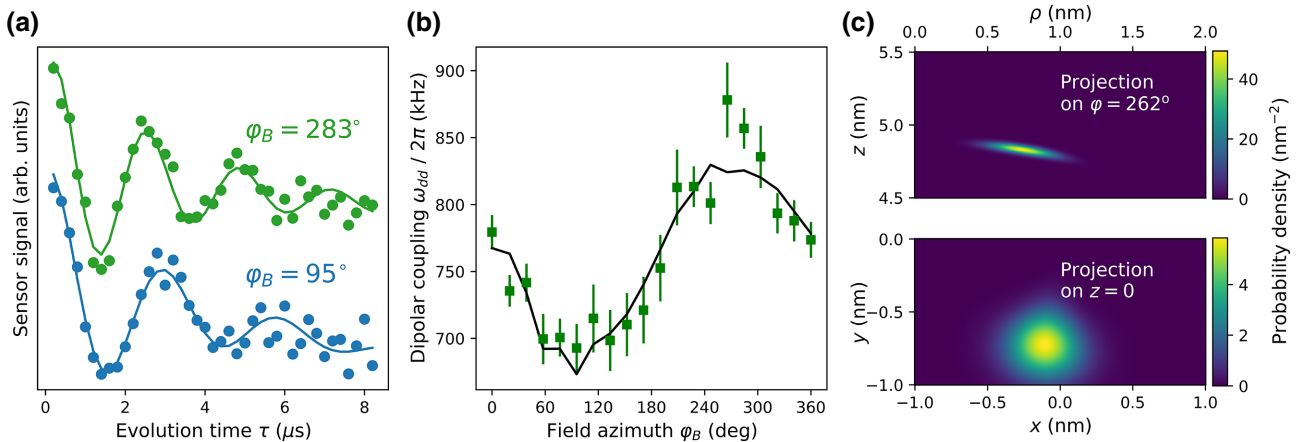


FIG. 3. Locating a spin by magnetic tomography. (a) Examples of dipolar coupling measurements for two different magnetic field azimuths φ_B , exhibiting two distinct dipolar coupling frequencies. The lines are fits to $f(\tau) = A \sin(\frac{1}{2}\omega_{dd}\tau + \phi) e^{-\frac{\tau}{T_2}}$. (b) The dipolar coupling frequency as a function of the magnetic field azimuth φ_B , oscillating over a single period. The black line is a fit to Eq. (3), incorporating variations in θ_B . We extract the target spin coordinates (r, θ, φ) from the fit. (c),(d) Probability maps for the position of the target spin, as extracted from the data in (b), presented in a ρ - z plot ($\rho \equiv \sqrt{x^2 + y^2}$) and an x - y plot.

ω_{dd} is a function of only φ_B (for details on data fitting, see the Supplemental Material [28]). From the fit, we obtain the target spin coordinates:

$$r = 4.89 \pm 0.02 \text{ nm}; \theta = 9.0 \pm 0.9^\circ; \varphi = -98 \pm 6^\circ. \quad (4)$$

We repeat the experiment for several trajectories of the magnet, corresponding to different values of magnetic field tilt θ_B . The ω_{dd} modulation gradually increases for larger field tilts, consistent with Eq. (3) (for the data, see the Supplemental Material [28]).

IV. SPIN-LOCATION PRECISION

To quantify the precision of the measurement, we define a location uncertainty based on the coordinate uncertainties obtained when fitting data to Eq. (3):

$$\Delta R \equiv (8r^2 \sin(\theta) \Delta r \Delta \theta \Delta \varphi)^{\frac{1}{3}}, \quad (5)$$

where Δx_i is the interval of confidence for coordinate x_i .

From the fit of the experimental data [Fig. 3(b)], we estimate the uncertainty of the target spin position to be $\Delta R = 0.09 \text{ nm}$. Figure 3(c) depicts the target-spin-position probability map. The largest uncertainty is along the $\hat{\varphi}$ axis, with $r \sin(\theta) \Delta \varphi = 0.09 \text{ nm}$.

To study the relevance of the method, we study the dependence of the location precision ΔR on the position of the spin and the characteristics of the sensor. Underlying ΔR is the dipolar frequency sensitivity, which depends on the system parameters (e.g., the sensor decoherence time T_2) and the specific protocol [30]. To focus the discussion on unique aspects of this measurement, we assume a given frequency uncertainty $\Delta\omega_{dd}$ and calculate the dependence of the uncertainty on the position of a target spin. The location uncertainty is proportional to the frequency uncertainty ($\Delta R \propto \Delta\omega_{dd}$), so the functional dependence of $\Delta R(\mathbf{r})$ is independent of the choice of $\Delta\omega_{dd}$. For the discussion, we use $\Delta\omega_{dd} = 2\pi \times 20 \text{ kHz}$ (in our experiment, the uncertainty is in the range of 12–28 kHz) and calculate $\Delta R(r, \theta)$, plotted in Fig. 4. Due to the symmetry of $\omega_{dd}(\mathbf{r}, \hat{\mathbf{b}})$, ΔR does not depend on the azimuth φ of the target spin.

We find that the uncertainty is minimal for $\theta \rightarrow 0$ and maximal for $\theta \rightarrow 90^\circ$. At $\theta = 90^\circ$, the second term of Eq. (3) vanishes, eliminating the information on the azimuth φ of the spin, such that for spins near $\theta = 90^\circ$, we can infer only the distance r and polar angle θ . Also, Eq. (3) is centrosymmetric, so there will always be (at least) two solutions for every data set. In many scenarios, however, these ambiguities may be resolved with prior information on the system. For example, when imaging a sample on the surface of the crystal, target spins will be in a thin slice on the surface, within a single hemisphere

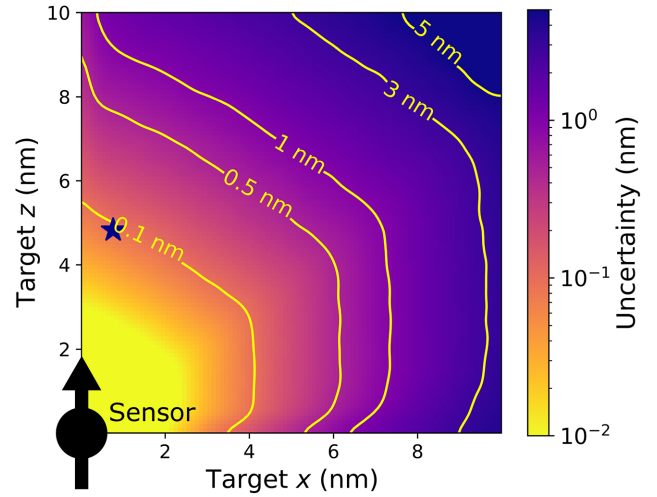


FIG. 4. The location precision of the electron spins. The location uncertainty ΔR versus the target spin coordinates ($x = r \sin \theta$, $z = r \cos \theta$), assuming $\Delta\omega_{dd} = 20 \text{ kHz}$. The contours denote equal levels of uncertainty. The blue star marks the spin position of the experiment.

around the sensor [7]. Nonetheless, target spins over 10 nm away from the sensor in the range of $\theta \in [0, 45^\circ]$ may be located with a precision better than 2 nm. This fact makes it appealing to use sensors the axis of which is normal to the surface, e.g., an N-V center in a diamond crystal cut along the (111) crystal plane [31].

The protocol is based on a tilted magnetic field and we also explore the impact of the field parameters—the magnitude B_0 and the tilt θ_B —for the case of an N-V-center sensor. The function of the N-V center as a magnetometer usually relies on an optical measurement of the spin state within a two-state subspace of the spin-1 states, e.g., $|m_s = 0\rangle$, $|m_s = +1\rangle$. The optical contrast between the states is maximal for a field aligned with the zero-field splitting axis of the center and decreases in the presence of a transverse field [29]. As the measurement requires a transverse magnetic field to modulate the dipolar coupling, there is a competition between the modulation amplitude and the contrast drop. To find the optimal conditions, we calculate the uncertainty as a function of the magnetic field B_0 and the field tilt angle θ_B and incorporate the optical contrast. At fields near 500 G, there is a sharp decrease in contrast for any finite transverse field and the uncertainty is large. For any field satisfying the condition $\mathcal{H}_{dd} \ll \omega_0 \ll D$, the dipolar coupling modulation amplitude does not depend on B_0 but only on θ_B . The criterion is satisfied for $B_0 \gtrsim 10 \text{ G}$ and so we calculate the expected uncertainty by solving the Hamiltonian of the system. We find that the uncertainty is minimized for a maximal tilt of $\theta_B \approx 85^\circ$ and minimal field $B_0 \sim 10 \text{ G}$ (for details, see the Supplemental Material [28]).

V. APPLICABILITY TO NITROXIDE SPIN LABELS

So far, we have discussed locating an electron spin that does not interact with nuclear spins. However, in many scenarios, the target electron spin may have significant interactions with nearby nuclear spins, as is the case with nitroxide radicals, the most common type of spin labels. Adding a hyperfine interaction term with a nucleus, $\mathbf{S}_e \cdot \mathbb{A}_{hf} \cdot \mathbf{I}$, modifies the spin Hamiltonian [Eq. (1)]. We expect a subsequent modification to $\omega_{dd}(\mathbf{r}, \hat{\mathbf{b}})$ [Eq. (3)], as the assumption that the Zeeman term dominates the eigenstates of the target spin is no longer valid.

For this discussion, we focus on the case of nitroxide radicals, where the electron spin is coupled by hyperfine constants of approximately $2\pi \times 100$ MHz to the adjacent nitrogen nuclear spin (^{14}N or ^{15}N) [32]. At fields of tens of gauss, the hyperfine term is comparable to $\gamma_e B_0$. We study the applicability of the magnetic tomography method to nitroxide spin labels by numerically simulating a magnetic azimuth sweep of the dipolar coupling between an N- V sensor and a nitroxide spin label. We use typical hyperfine coupling parameters for a nitroxide radical with an ^{14}N nuclear spin ($A_{\parallel} = 2\pi \times 101.4$ MHz, $A_{\perp} = 2\pi \times 14.7$ MHz) [32].

We calculate the modulation of the dipolar coupling with a spin label at an arbitrary position and orientation, under B_0 fields in the range of 20–100 G. We assume that the spin label is in a thermal state of the nuclear spin, i.e., equal probabilities of the nucleus spin-1 states. The simulations are presented in Fig. 5 and compared with the theoretical model for $\omega_{dd}(\mathbf{r}, \hat{\mathbf{b}})$ [Eq. (3)]. At 20 G, the simulated azimuth sweep deviates significantly from the

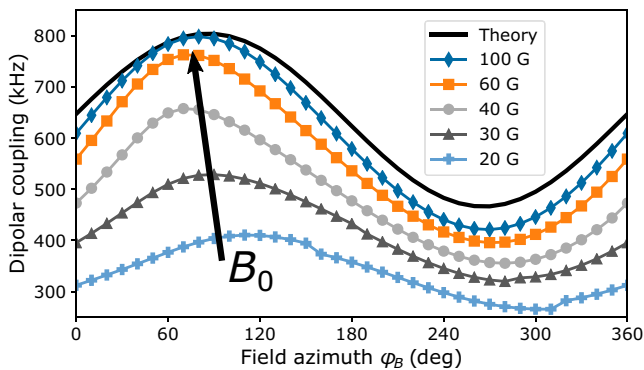


FIG. 5. The magnetic azimuth sweep of nitroxide spin labels. A comparison of numerically calculated azimuth sweeps of a nitroxide radical (^{14}N) at different field magnitudes. The electron spin is arbitrarily positioned, with an arbitrary orientation of the hyperfine axes. The curves are compared to the theoretical model for $\omega_{dd}(\mathbf{r}, \hat{\mathbf{b}})$. At $B_0 \gtrsim 100$ G, the calculated curve is well approximated by the theoretical model.

model and approaches it gradually for higher fields. At a field of $B_0 = 100$ G the simulated curve is well approximated by the theoretical model. While a field of 100 G entails a decrease in precision due to the transverse field, our calculations show that it allows mapping spins with Ångstrom precision (see the Supplemental Material [28]). For the case of a hyperfine coupled spin, however, a more precise location estimation may be obtained by fitting to a calculated $\omega_{dd}(\mathbf{r}, \mathbf{B})$, instead of the analytical term.

The magnetic tomography model $\omega_{dd}(\mathbf{r}, \hat{\mathbf{b}})$ of Eq. (3) applies for a hyperfine coupled spin already at a moderate field of 100 G, despite the Zeeman term being on the same order of magnitude as the hyperfine parameter ($A_{\parallel} \approx 2\pi \times 101.4$ MHz $\sim \gamma_e B_0 \approx 2\pi \times 280$ MHz) and thus not being negligible. This stems from the fact that, for a thermal ensemble of the nuclear spin states at 100 G, the expectation value of the target electron spin operator perpendicular to the field axis $\hat{\mathbf{b}}$ satisfies $|\langle S_e^{\perp} \rangle| / \langle S_e^{\parallel} \rangle \ll 1$ (see the Supplemental Material [28]). It follows that the secular approximation holds for this scenario as well and so Eq. (3) constitutes a valid approximation. Thus, the magnetic tomography method may also be applicable to mapping nitroxide spin labels and other similar hyperfine-coupled electron spins.

VI. DISCUSSION AND CONCLUSIONS

N- V centers in diamond are a leading platform for nanoscale magnetometry, particularly for single-molecule magnetic resonance tasks. Here, we demonstrate a method for mapping the locations of spins in the vicinity of an N- V -center sensor with Ångstrom-scale precision. The location precision of the spin that we demonstrate here is one order of magnitude higher than previously reported for a similar magnetic-field-scanning experiment (approximately 1 nm) [20] and a spin-imaging technique based on a scanning magnetic tip (1.5 nm) [16]. Magnetic resonance imaging demonstrated recently with a scanning tunneling microscope has exhibited superior precision but requires strict conditions [15,33]. Notably, the magnetic tomography method does not require a scanning probe setup, which is operationally complex, and the method is operable at both ambient and cryogenic conditions.

Spin mapping with Ångstrom resolution may provide added value for applications such as single-molecule distance measurements. For this, we would measure the positions of a pair of spin labels attached to a biomolecule, from which we can infer the distance. To do so, the dipolar coupling to each spin needs to be measured as a function of the magnetic field direction and fitted to $\omega_{dd}(\mathbf{r}, \hat{\mathbf{b}})$ [Eq. (3)]. A minimal frequency resolution is needed to distinguish between the dipolar coupling of two or more spins and it is given by the coherence time of the sensor $\delta\omega \sim$

$1/T_2$. Another approach is selective addressing by separating the electron spin resonances of the targets, which allows measurement of the dipolar coupling of each spin separately [21]. Selective addressing may also be achieved by attaching spin labels with distinct resonance spectra, such as nitroxide radicals with different nitrogen isotopes (^{14}N , ^{15}N) [34,35].

The uncertainty of the measurement is proportional to the frequency-estimation uncertainty, so techniques that lengthen the coherence time and improve the sensor read-out efficiency would enhance the spin-location precision. Nonetheless, with nanometer precision up to 10 nm away from the sensor, the method can be used for sensing spin labels on molecules external to the diamond crystal. Thus, the magnetic tomography method is relevant for studying the structure of individual molecules by spin-label distance measurements or high-resolution characterization of quantum spin networks.

ACKNOWLEDGMENTS

We acknowledge Leora Schein-Lubomirsky for contributions to the experimental setup and for calculations. We thank Alon Salhov for ideas and fruitful comments. It is a pleasure to thank Durga Dasari for insightful discussions. A.F. is the incumbent of the Elaine Blond Career Development Chair and acknowledges the historic generosity of the Harold Perlman Family, research grants from the Abramson Family Center for Young Scientists and the Willner Family Leadership Institute for the Weizmann Institute of Science, as well as support from the Israel Science Foundation (Grants No. ISF 963/19 and No. ISF 419/20).

-
- [1] O. Schiemann and T. F. Prisner, Long-range distance determinations in biomacromolecules by EPR spectroscopy, *Q. Rev. Biophys.* **40**, 1 (2007).
 - [2] D. Marion, An introduction to biological NMR spectroscopy, *Mol. Cell. Proteomics* **12**, 3006 (2013).
 - [3] G. Jeschke, DEER distance measurements on proteins, *Annu. Rev. Phys. Chem.* **63**, 419 (2012).
 - [4] W. L. Hubbell, C. J. López, C. Altenbach, and Z. Yang, Technological advances in site-directed spin labeling of proteins, *Curr. Opin. Struct. Biol.* **23**, 725 (2013).
 - [5] L. Rondin, J. P. Tetienne, P. Spinicelli, C. Dal Savio, K. Karrai, G. Dantelle, A. Thiaville, S. Rohart, J. F. Roch, and V. Jacques, Nanoscale magnetic field mapping with a single spin scanning probe magnetometer, *Appl. Phys. Lett.* **100**, 153118 (2012).
 - [6] J. Cai, F. Jelezko, M. B. Plenio, and A. Retzker, Diamond-based single-molecule magnetic resonance spectroscopy, *New J. Phys.* **15**, 013020 (2013).
 - [7] T. Staudacher, F. Shi, S. Pezzagna, J. Meijer, J. Du, C. A. Meriles, F. Reinhard, and J. Wrachtrup, Nuclear magnetic resonance spectroscopy on a (5-nanometer)³ sample volume, *Science* **339**, 561 (2013).
 - [8] H. J. Mamin, M. Kim, M. H. Sherwood, C. T. Rettner, K. Ohno, D. D. Awschalom, and D. Rugar, Nanoscale nuclear magnetic resonance with a nitrogen-vacancy spin sensor, *Science* **339**, 557 (2013).
 - [9] I. Lovchinsky, A. O. Sushkov, E. Urbach, N. P. de Leon, S. Choi, K. De Greve, R. Evans, R. Gertner, E. Bersin, C. Muller, L. McGuinness, F. Jelezko, R. L. Walsworth, H. Park, and M. D. Lukin, Nuclear magnetic resonance detection and spectroscopy of single proteins using quantum logic, *Science* **351**, 836 (2016).
 - [10] F. Shi, Q. Zhang, P. Wang, H. Sun, J. Wang, X. Rong, M. Chen, C. Ju, F. Reinhard, H. Chen, J. Wrachtrup, J. Wang, and J. Du, Single-protein spin resonance spectroscopy under ambient conditions, *Science* **347**, 1135 (2015).
 - [11] L. Schlipf, T. Oeckinghaus, K. Xu, D. B. R. Dasari, A. Zappe, F. F. de Oliveira, B. Kern, M. Azarkh, M. Drescher, M. Ternes, K. Kern, J. Wrachtrup, and A. Finkler, A molecular quantum spin network controlled by a single qubit, *Sci. Adv.* **3**, e1701116 (2017).
 - [12] M. R. Wasielewski, M. D. E. Forbes, N. L. Frank, K. Kowalski, G. D. Scholes, J. Yuen-Zhou, M. A. Baldo, D. E. Freedman, R. H. Goldsmith, T. Goodson, M. L. Kirk, J. K. McCusker, J. P. Ogilvie, D. A. Shultz, S. Stoll, and K. B. Whaley, Exploiting chemistry and molecular systems for quantum information science, *Nat. Rev. Chem.* **4**, 490 (2020).
 - [13] D. Rugar, R. Budakian, H. J. Mamin, and B. W. Chui, Single spin detection by magnetic resonance force microscopy, *Nature* **430**, 329 (2004).
 - [14] C. Durkan and M. E. Welland, Electronic spin detection in molecules using scanning-tunneling-microscopy-assisted electron-spin resonance, *Appl. Phys. Lett.* **80**, 458 (2002).
 - [15] P. Willke, K. Yang, Y. Bae, A. J. Heinrich, and C. P. Lutz, Magnetic resonance imaging of single atoms on a surface, *Nat. Phys.* **15**, 1005 (2019).
 - [16] M. S. Grinolds, M. Warner, K. De Greve, Y. Dovzhenko, L. Thiel, R. L. Walsworth, S. Hong, P. Maletinsky, and A. Yacoby, Subnanometre resolution in three-dimensional magnetic resonance imaging of individual dark spins, *Nat. Nanotechnol.* **9**, 279 (2014).
 - [17] M. H. Abobeih, J. Randall, C. E. Bradley, H. P. Bartling, M. A. Bakker, M. J. Degen, M. Markham, D. J. Twitchen, and T. H. Taminiau, Atomic-scale imaging of a 27-nuclear-spin cluster using a single-spin quantum sensor, *Nature* **576**, 411 (2019).
 - [18] J. Zopes, K. Herb, K. S. Cujia, and C. L. Degen, Three-Dimensional Nuclear Spin Positioning Using Coherent Radio-Frequency Control, *Phys. Rev. Lett.* **121**, 170801 (2018).
 - [19] K. S. Cujia, K. Herb, J. Zopes, J. M. Abendroth, and C. L. Degen, Parallel detection and spatial mapping of large nuclear spin clusters, *Nat. Commun.* **13**, 1260 (2021).
 - [20] A. O. Sushkov, I. Lovchinsky, N. Chisholm, R. L. Walsworth, H. Park, and M. D. Lukin, Magnetic Resonance Detection of Individual Proton Spins Using Quantum Reporters, *Phys. Rev. Lett.* **113**, 197601 (2014).
 - [21] A. Cooper, W. K. C. Sun, J. C. Jaskula, and P. Cappellaro, Identification and Control of Electron-Nuclear Spin Defects in Diamond, *Phys. Rev. Lett.* **124**, 083602 (2020).
 - [22] A. Kak, Computerized tomography with X-ray, emission, and ultrasound sources, *Proc. IEEE* **67**, 1245 (1979).

- [23] R. Nagy, M. Niethammer, M. Widmann, Y.-C. Chen, P. Udvarhelyi, C. Bonato, J. U. Hassan, R. Karhu, I. G. Ivanov, N. T. Son, J. R. Maze, T. Ohshima, Öney O. Soykal, Á. Gali, S.-Y. Lee, F. Kaiser, and J. Wrachtrup, High-fidelity spin and optical control of single silicon-vacancy centres in silicon carbide, *Nat. Commun.* **10**, 1954 (2019).
- [24] G. Jeschke, Distance measurements in the nanometer range by pulse EPR, *Chemphyschem* **3**, 927 (2002).
- [25] B. Grotz, J. Beck, P. Neumann, B. Naydenov, R. Reuter, F. Reinhard, F. Jelezko, J. Wrachtrup, D. Schweinfurth, B. Sarkar, and P. Hemmer, Sensing external spins with nitrogen-vacancy diamond, *New J. Phys.* **13**, 055004 (2011).
- [26] P. Neumann, R. Kolesov, B. Naydenov, J. Beck, F. Rempp, M. Steiner, V. Jacques, G. Balasubramanian, M. L. Markham, D. J. Twitchen, S. Pezzagna, J. Meijer, J. Twamley, F. Jelezko, and J. Wrachtrup, Quantum register based on coupled electron spins in a room-temperature solid, *Nat. Phys.* **6**, 249 (2010).
- [27] H. J. Mamin, M. H. Sherwood, and D. Rugar, Detecting external electron spins using nitrogen-vacancy centers, *Phys. Rev. B* **86**, 195422 (2012).
- [28] See the Supplemental Material at <http://link.aps.org/supplemental/10.1103/PhysRevApplied.18.054016> for information on experimental methods, data analysis, and simulations.
- [29] J. P. Tetienne, L. Rondin, P. Spinicelli, M. Chipaux, T. Debuisschert, J. F. Roch, and V. Jacques, Magnetic-field-dependent photodynamics of single NV defects in diamond: An application to qualitative all-optical magnetic imaging, *New J. Phys.* **14**, 103033 (2012).
- [30] C. L. Degen, F. Reinhard, and P. Cappellaro, Quantum sensing, *Rev. Mod. Phys.* **89**, 035002 (2017).
- [31] J. Michl, T. Teraji, S. Zaiser, I. Jakobi, G. Waldherr, F. Dolde, P. Neumann, M. W. Doherty, N. B. Manson, J. Isoya, and J. Wrachtrup, Perfect alignment and preferential orientation of nitrogen-vacancy centers during chemical vapor deposition diamond growth on (111) surfaces, *Appl. Phys. Lett.* **104**, 102407 (2014).
- [32] D. Marsh, *Spin-Label Electron Paramagnetic Resonance Spectroscopy* (CRC Press, Boca Raton, 2019).
- [33] P. Willke, T. Bilgeri, X. Zhang, Y. Wang, C. Wolf, H. Aubin, A. Heinrich, and T. Choi, Coherent spin control of single molecules on a surface, *ACS Nano* **15**, 17959 (2021).
- [34] S. Lee, T. C. Sandreczki, and I. M. Brown, Analyses of the electron-spin-resonance (ESR) hyperfine powder spectra of nitroxide radicals enriched with ^{15}N ($I = 1/2$), *J. Chem. Phys.* **80**, 3983 (1984).
- [35] C. Munuera-Javaloy, R. Puebla, B. D'Anjou, M. B. Plenio, and J. Casanova, Detection of molecular transitions with nitrogen-vacancy centers and electron-spin labels, [arXiv:2110.14255](https://arxiv.org/abs/2110.14255) (2021), deposited on the arXiv.
- [36] S. Sangtawesin, B. L. Dwyer, S. Srinivasan, J. J. Allred, L. V. Rodgers, K. De Greve, A. Stacey, N. Dontschuk, K. M. O'Donnell, D. Hu, D. A. Evans, C. Jaye, D. A. Fischer, M. L. Markham, D. J. Twitchen, H. Park, M. D. Lukin, and N. P. De Leon, Origins of Diamond Surface Noise Probed by Correlating Single-Spin Measurements with Surface Spectroscopy, *Phys. Rev. X* **9**, 031052 (2019).
- [37] J. M. Binder, A. Stark, N. Tomek, J. Scheuer, F. Frank, K. D. Jahnke, C. Müller, S. Schmitt, M. H. Metsch, T. Uden, T. Gehring, A. Huck, U. L. Andersen, L. J. Rogers, and F. Jelezko, Qudi: A modular PYTHON suite for experiment control and data processing, *SoftwareX* **6**, 85 (2017).
- [38] I. Aharonovich, S. Castelletto, D. A. Simpson, C.-H. Su, A. D. Greentree, and S. Praver, Diamond-based single-photon emitters, *Rep. Prog. Phys.* **74**, 076501 (2011).
- [39] A. Schweiger and G. Jeschke, *Principles of Pulse Electron Paramagnetic Resonance* (Oxford University Press on Demand, New York, 2001).
- [40] B. J. Maertz, A. P. Wijnheijmer, G. D. Fuchs, M. E. Nowakowski, and D. D. Awschalom, Vector magnetic field microscopy using nitrogen vacancy centers in diamond, *Appl. Phys. Lett.* **96**, 092504 (2010).